minerals

MDPI

Article

Characterization of Limestone Surface Impurities and Resulting Quicklime Quality

Karin Sandström [1,2,3], Markus Carlborg [1,2], Matias Eriksson [1,2,4,*] and Markus Broström [1,2]

[1] Centre for Sustainable Cement and Quicklime Production, Department of Applied Physics and Electronics, Umeå University, SE-901 87 Umeå, Sweden; karin.sandstrom@umu.se (K.S.); markus.carlborg@umu.se (M.C.); markus.brostrom@umu.se (M.B.)
[2] Thermochemical Energy Conversion Laboratory, Department of Applied Physics and Electronics, Umeå University, SE-901 87 Umeå, Sweden
[3] Industrial Doctoral School for Research and Innovation, Umeå University, SE-901 87 Umeå, Sweden
[4] The Swedish Mineral Processing Research Association—MinFo, Marieviksgatan 25, SE-100 44 Stockholm, Sweden
* Correspondence: matias.eriksson@umu.se

Abstract: Quicklime, rich in CaO(s), is generated by calcining limestone at high temperatures. Parallel-flow regenerative lime kilns are the most energy-effective industrial method available today. To prevent major disruptions in such kilns, a high raw material quality is necessary. Under some conditions, impurity-enriched material may adhere to limestone pebbles and enter the kiln. In this study, limestone and corresponding quicklime were analyzed to evaluate the extent and composition of surface impurities and assess the effect on quicklime product quality, here defined as free CaO. This was performed by sampling and analyzing limestone, quarry clay, laboratory-produced quicklime, and industrially produced quicklime with XRF, SEM/EDX, and XRD; interpretations were supported by thermodynamic equilibrium calculations. In the laboratory-produced quicklime, the surface impurities reacted with calcium forming Larnite, Gehlenite, Åkermanite and Merwinite, reducing the quicklime quality. The results showed that the limestone surface layer comprised 1.2 wt.-% of the total mass but possessed 4 wt.-% of the total impurities. The effect on industrially produced quicklime quality was lower; this indicated that the limestone surface impurities were removed while the material moved through the kiln. Multicomponent chemical equilibrium calculations showed that the quarry clay was expected to be fully melted at 1170 °C, possibly leading to operational problems.

Keywords: clay minerals; parallel-flow regenerative kiln; twin-shaft regenerative kiln; free CaO; thermodynamic equilibrium calculations

Citation: Sandström, K.; Carlborg, M.; Eriksson, M.; Broström, M. Characterization of Limestone Surface Impurities and Resulting Quicklime Quality. *Minerals* **2024**, *14*, 608. https://doi.org/10.3390/min14060608

Academic Editor: Mercedes Suárez

Received: 8 May 2024
Revised: 7 June 2024
Accepted: 10 June 2024
Published: 13 June 2024

1. Introduction

The primary source of quicklime (solid rich in CaO(s)) is limestone, a sedimentary rock extracted through quarrying or mining. Limestone is naturally rich in calcium carbonate ($CaCO_3$), predominantly in the mineral Calcite. The manufacturing of quicklime is energy-demanding: Limestone is decomposed to quicklime at high temperatures in industrial lime kilns, typically shaft kilns or rotary kilns. The most energy-effective method available on the market is the twin-shaft parallel-flow regenerative kiln (PFR kiln); see a schematic representation in Figure 1. The energy requirement is around 3.2–4.2 MJ/kg of quicklime with a maximum quicklime temperature reaching around 1030 °C [1,2]. The shafts are filled, and the raw material enters the preheating zones at the top of the shafts, and quicklime is discharged at the bottom after passing the calcination and cooling zones. Around four to five times per hour, the burning alternates between shafts, and the hot gases from the burning shaft pass through a ring channel to the non-burning shaft. This setup enables high energy efficiency and the possibility to produce a uniform soft burnt quicklime with high quality. A disadvantage of this setup is that it requires a relatively high stone and fuel

quality to be able to operate without major disruptions [3]. Disruptions can be caused by block formations due to quicklime densification, agglomeration, and possibly melting. It can be related to non-uniform combustion or irregular energy consumption or caused by poor raw material quality, either as a high share of impurities or high thermal decrepitation of the limestone [4,5].

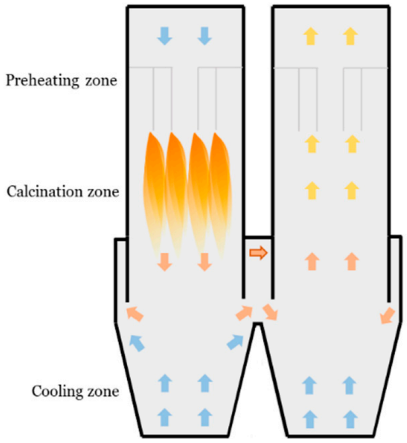

Figure 1. Schematic representation of the PFR kiln. Arrows denote air/gas directions. Color grading of arrows indicate air/gas temperature, where blue: cold air and red/yellow: hot gas. Adapted from [6].

Impurities found in limestone deposits can be classified into two groups, homogenous and heterogeneous. Homogenous impurities co-deposit with the limestone and are dispersed throughout the formation. Heterogeneous impurities appear as inclusions or as loosely embedded materials and are formed during the sedimentation process; they are seen as layers in the deposits [7–9]. Quicklime quality is influenced by factors like kiln configuration and fuel characteristics, but it is primarily influenced by the composition and characteristics of the raw material: the limestone feed rock [8,10]. In quicklime production, all other compounds in the raw material except $CaCO_3$(s) are considered impurities. Common impurities are clay and siliceous matter, and the major impurity elements are Si, Al, Fe, and Mg [8,11]. Limestone can be classified based on the chemical purity of the rock, where a chemically purer limestone, under similar production parameters, results in a chemically purer quicklime product. The following limestone classification is used: very high purity equivalent CaO content > 55.2 wt.-%, high purity 54.3 < CaO < 55.2 wt.-%, medium purity 52.4 < CaO < 54.3 wt.-%, low purity 47.6 < CaO < 52.4 wt.-%, and impure limestone for CaO < 47.6 wt.-% [12–14]. Table 1 presents typical ranges of impurities and trace elements found in commercial limestone used for quicklime production [9]. During limestone processing such as blasting, crushing, and sieving, a fine quarry dust usually enriched in impurities is formed. The experience of lime kiln operators suggests that the fine particulate material can adhere to the surface of limestone pebbles fed to the kiln to such an extent that it affects kiln operational stability. This is reported to be more prominent in cold and wet conditions. In a previous study, it was presented that the surface impurities can reduce the quicklime quality (defined as the level of free lime, CaO(s)) up to 1.5 wt.-% according to multicomponent chemical equilibrium calculations [15]. In addition, for every 1 wt.-% of impurities in the limestone kiln feed, a reduction in free CaO(s) up to 4 wt.-% can be expected as a result of both diluting and reacting with the CaO(s) in the quicklime. This effect is more prominent at high temperatures [8].

Table 1. Typical ranges of levels of impurities and trace elements in commercial limestone. Data from [8,9].

		Range
Silicon	wt.-%	0.005–0.9
Aluminium		0.01–0.4
Iron		0.007–0.2
Sulphur		0.002–0.01
Manganese	mg/kg	13–632
Antimony		0.1–3
Arsenic		0.1–15
Boron		1–50
Cadmium		0.1–1.5
Chromium		3–300
Copper		1–30
Fluoride		5–3000
Lead		0.5–30
Mercury		0.02–0.1
Molybdenum		0.1–30
Nickel		0.5–15
Selenium		0.02–3
Silver		0.2–4
Tin		0.1–15
Vanadium		1–50
Zinc		3–500

In the present study, the objective was to evaluate how surface impurities attached to limestone pebbles affect quicklime product quality, here defined as free CaO(s). This was performed by analyzing the elemental composition of the raw materials with XRF, the thickness of the surface layer and morphology of the surface layer with SEM/EDX, and the phase composition in limestone, quarry clay, industrially produced quicklime, and laboratory-produced quicklime with XRD.

2. Materials and Methods

The limestone used in this study (LS) originates from a sedimentary deposit. The limestone deposit consists of 35–40 m thick strata on top of a layer of marlstone. The limestone stratum itself consists of different defined structures. In the bottom of the deposit, a layer of crinoid limestone is present, and the top layer consists of stromatoporoid limestone. In addition, elements of reef limestone that form defined bodies are present. Erosion from the reef limestone, present as fragment limestone, surrounds the defined bodies. Clay minerals are present as thin layers in of crinoid, stromatoporoid, and reef limestone, with a thickness ranging from mm scale up to 0.5–1 m. The clay minerals originate from weathered metamorphic bedrock that has been deposited during the formation of the limestone strata in deep, warm, and calm water. A schematic view of the deposit is presented in Figure 2. LS was collected during a period of moist weather and the elemental composition is presented in Table 2 (as received). It is classified as a medium-purity limestone [12–14].

Table 2. Analysis results of $LS_{as\ received}$, LS_{washed}, $LS_{washing\ residue}$, and QC, in wt.-%, determined by XRF, IR-S, and LOI at 950 °C.

	$LS_{as\ received}$ [1]	**LS_{washed}**	**$LS_{washing\ residue}$**	**QC**
CaO	52.79	53.13	47.88	17.93
MgO	1.02	1.08	2.62	5.58
SiO_2	1.39	1.36	4.75	28.46
Al_2O_3	0.59	0.59	2.18	14.03
Fe_2O_3	0.32	0.27	0.93	5.08

Table 2. *Cont.*

	$LS_{as\ received}$ [1]	LS_{washed}	$LS_{washing\ residue}$	QC
Mn_2O_3	n.a.	0.02	0.03	0.05
P_2O_5	n.a.	<0.00	0.02	0.03
Na_2O	n.a.	0.00	0.04	0.40
TiO_2	n.a.	0.03	0.12	0.79
K_2O	0.15	0.15	0.63	4.27
S	0.08	0.03	0.15	1.05
LOI	42.94	42.90	40.22	20.84
Sum [wt.-%]	99.3	99.5	99.6	98.5
Share [%]	100	98.8	1.2	
Impurities (ton/month)		945	35	
Share of impurities [%]		96	4	

[1] Performed by the limestone sample provider and corresponds to an average of 30 days. n.a. = not analyzed.

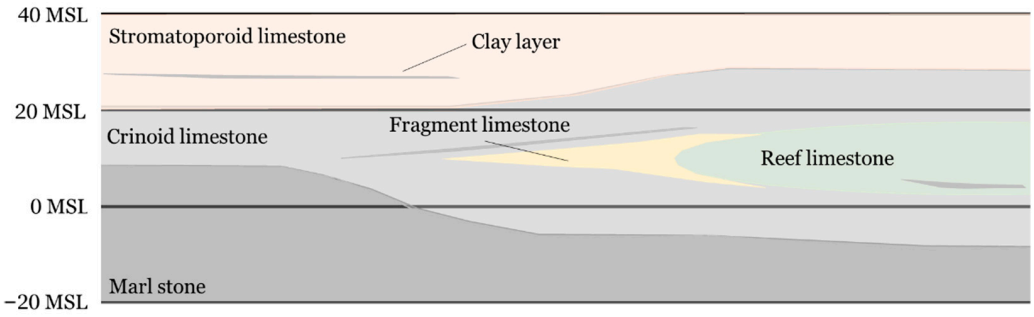

Figure 2. Schematic view of the limestone deposit. Clay minerals are present in all parts of the deposit except the fragment limestone. MSL: Meters above Sea Level.

To investigate the amount and composition of surface impurities, a representative sample of 17 kg limestone was washed by mechanical surface cleaning through scrubbing the 40–90 mm pebbles in de-ionized water in a 15 L cylindrical drum. The surface material settled, and the excess water was decanted before drying at 105 °C. The procedure is also described elsewhere [15]. The washed limestone pebbles (LS_{washed}) and the washing residue ($LS_{washing\ residue}$) were weighed before further analysis. Based on a nominal quicklime production rate of 450 tons quicklime/day (tpd), the total weight of material in each fraction/month was calculated as

$$W_{washing\ residue/washed}\left[\frac{ton}{months}\right] = \frac{450\left[\frac{ton\ QL}{day}\right]\cdot 30\left[\frac{days}{month}\right]\cdot 1.786\left[\frac{ton\ LS}{ton\ QL}\right]\cdot wt.-\%_{washing\ residue/washed}}{100}, \quad (1)$$

where 1.786 represents the weight-factor from quicklime to limestone and $wt.-\%_{washing\ residue/washed}$ represents the share of each fraction from the washing procedure. The amount of impurities in each fraction was calculated as

$$W_{Impurities\ in\ washing\ residue/washed}\left[\frac{ton}{months}\right] = \frac{W_{washing\ residue/washed}\left[\frac{ton}{months}\right]\cdot(100 - LOI\ [\%] - CaO[\%])}{100}, \quad (2)$$

assuming that everything except CaO(s) and loss on ignition (LOI) was impurities.

A representative sample of the quarry clay (QC), originating from the LS quarry was gathered manually from different heterogenous clay layers occurring in the vertical quarry wall at fresh bench fronts at an approximate depth of 6 m from the surface. The samples were then consolidated into one composite sample and served as a reference for the quarry clay composition.

2.1. Quicklime Samples

Laboratory-produced quicklime (LPQ) was produced by heating LS-pebbles to 1100 °C in a muffle furnace. The maximum heating rate was 10 °C/minute, and the samples were held for 4 h at the set temperature. The gas atmosphere was 25 vol.-% CO_2 and 75 vol.-% air with a flow rate of one furnace volume/minute. The samples were slowly cooled in the furnace in a flow of N_2 gas to avoid recarbonation and hydration. The total weight loss was 43–44 wt.-% for all the samples, indicating complete calcination. In Figure 3, a thick layer is visible on the surface of an LPQ pebble; this area was manually peeled off and further analyzed.

Figure 3. Laboratory-produced quicklime sample after calcination. Surface layer partially covering the surface is marked with yellow arrow.

The industrially produced quicklime sample (IPQ) was gathered from a PFR kiln fed with LS as kiln feed. The nominal quicklime production rate was 450 tpd. The raw material pebble size was 40–90 mm. Flue gases typically consist of 12–13 vol-% CO_2. The kiln was fired with fuel oil containing less than 1.0 wt.-% ash, and the ash content was assumed to be negligible. Since the ash content was assumed to be negligible, the influence of the ash on quicklime product quality was not investigated in this work.

Typical $CaCO_3$ content in lime kiln feed was around 97 wt.-%, corresponding to an equivalent CaO of around 54.3 wt.-%. However, the limestone investigated in this study was collected during a period of moist weather, and the average $CaCO_3$ content during the 30 days was 96.3 ± 0.5 wt.-% (n = 30), corresponding to an equivalent CaO of around 53.9 wt.-%. During the period, the operators reported a lower temperature in the preheating zone, an increased amount of lime kiln dust in the flue gas filter, and a high blocking tendency in the ring channel. The quicklime quality was determined by available CaO as 88.5 wt.-% and residual CO_2-content as 1.2 wt.-% during the 30 days.

2.2. Analytical Methods

XRF analysis is a way of determining the elemental composition in solid materials and has been used extensively to characterize limestone materials previously; see, for example, [4,5,16]. In this study, XRF was performed with an ARL Perform'x model GEN-X 2500 W, Thermo Fisher Scientific (Waltham, MA, USA) on $LS_{\text{as received}}$, QC, LS_{washed}, and $LS_{\text{washing residue}}$ for average elemental composition. The sulfur content was determined with Leco CS744 (LECO Europe B.V, Geleen, The Netherlands). LOI was gravimetrically determined at 950 °C.

Scanning Electron Microscopy coupled with Energy-Dispersive X-ray spectroscopy (SEM/EDX, Zeiss EVO LS15) (Carl Zeiss AG, Baden-Wurttemberg, Germany) was used to compare the morphology and relative elemental composition of surface impurities in the LS, LPQ, and IPQ samples. The SEM/EDX used a LaB6 electron source operating at an extended pressure of 50–60 Pa with an acceleration voltage of 15 kV and a probe current of 500–700 pA. This method has been used previously to determine the morphology and elemental composition of both limestone and quicklime materials [4,5,17,18].

Crystalline phases in $LS_{washing\ residue}$, QC, and the surface layers of IPQ and LPQ were analyzed with Powder X-ray diffraction (XRD). For LPQ, its visible surface layer, as pointed out in Figure 3, was manually peeled off. The surface layer of IPQ was removed with a steel brush. LPQ and IPQ were analyzed with Bruker AXS d8 advance (Bruker, Billerica, MA, USA) operating in a 2θ mode with Cu-Kα radiation and a spinning sample. $LS_{washing\ residue}$ and QC were analyzed with a Malvern PANalytical, X'pert^3 operating in 2θ mode with Cu-Kα radiation on a spinning sample (Malvern Panalytical Ltd, Malvern, UK). The diffractograms were matched against references in the PDF-4 2023 database [19] and semi-quantification of the identified phases was obtained with Rietveld refinement in Topas 4.2 provided by Bruker. The crystal structure references used for Rietveld refinement are listed in Appendix A.

2.3. Multicomponent Chemical Equilibrium Calculations

To estimate the share of melt in $LS_{as\ received}$, LS_{washed}, $LS_{washing\ residue}$, and QC at high temperature, multicomponent chemical equilibrium calculations based on the XRF results were performed between 700 and 1400 °C. Factsage 8.2 with the commercially available databases FToxid and FactPS, a customized database for salt melt and a customized database for alite formation in systems with relatively high MgO concentrations, was utilized for this purpose [20–22]. The models used for melt and solid solutions were as follows: A-slag liq (P and S excluded), Bred, bC2SC, aC2SB, OlivA, C2AF, C3AF, Maxi-alkH, Maxi-Salt, Maxi-Hexa, Maxi-Fair, and Maxi-glas. The elements used in the calculations were Al, Ca, Fe, K, Mg, Mn, Na, P, Si, Ti, and C, H, N, O, and S. The calculations were performed with methane and air (N_2 and O_2), with O_2 levels at around 3% in the gas phase.

3. Results and Discussion

Quicklime has many quality parameters, such as reactivity [23], available lime, and CO_2 content [24]. In the present study, the chemical quality of the quicklime pebbles is discussed in terms of the amount of free CaO(s) as affected by the impurities attached to the surface of the limestone pebbles.

3.1. Elemental Composition of Raw Materials

The elemental composition of $LS_{as\ received}$, LS_{washed}, $LS_{washing\ residue}$, and QC determined by XRF, IR-S analysis, and LOI, are presented in Table 2 together with the share of LS_{washed} and $LS_{washing\ residue}$. The elemental composition of $LS_{as\ received}$ represents the average composition of 24,000 tons of limestone consumed during the 30-day kiln period. The composition allows for chemical classification based on purity according to [12–14]. $LS_{as\ received}$ and LS_{washed} both represented medium-purity limestone. However, the impurities decreased the CaO content in the bulk feed by approximately 0.3 units of wt.-% from 53.13 wt.-% in LS_{washed} to 52.79 wt.-% in $LS_{as\ received}$. The analyzed surface layer, $LS_{washing\ residue}$, represented impure limestone (CaO content 47.88 wt.-%), and the impurities comprised mainly MgO, SiO_2, Al_2O_3, Fe_2O_3, and K_2O (expressed as oxides).

Based on the washing and weighing, it was determined that LS_{washed} consisted of 98.8 wt.-% of the total limestone mass and that $LS_{washing\ residue}$ consisted of 1.2 wt.-% of the total limestone mass. Based on the LOI and CaO content from the XRF analysis, LS_{washed} and $LS_{washing\ residue}$ were determined to contain a monthly load of 945 and 35 tons of impurities, respectively.

The CaO content in QC was 17.93 wt.-%, and the impurities consisted mainly of MgO, SiO_2, Al_2O_3, Fe_2O_3, and K_2O (expressed as oxides). The same elements were found in elevated levels in $LS_{washing,\ residue,}$ indicating that the origin of the impurities was the same.

3.2. Morphology, Elemental Distribution, and Phase Composition of Raw Materials

The relative average elemental distribution of the LS surface layer is presented in Table 3. It was determined with SEM/EDX on an oxygen, chlorine, and carbon-free basis and expressed as oxides. Areas 1, 2, and 3 in Figure 4 represent different morphologies: 1 represents bulk limestone, 2 represents coarse-grained surface impurities, and 3 represents fine-grained surface impurities. The morphology is visualized in Figure 4a (middle).

Table 3. Relative average elemental composition detected in bulk and surface areas analyzed with SEM/EDX, as exemplified in Figure 4 (wt.-%). Values reported on oxygen, chlorine, and carbon-free basis and expressed as wt.-% oxides.

wt.-%	**LS**			**LPQ**			**IPQ**	
	Area 1 (*n* = 11)	**Area 2 (*n* = 16)**	**Area 3 (*n* = 10)**	**Area 1 (*n* = 9)**	**Area 2 (*n* = 14)**	**Area 3 (*n* = 9)**	**Area 1 (*n* = 8)**	**Area 2 (*n* = 8)**
CaO	95.2	79.0	54.5	96.9	82.7	48.8	95.4	76.1
MgO	1.2	4.0	6.4	1.1	4.3	20.7	1.2	3.3
SiO_2	2.5	10.1	23.0	1.3	8.0	18.2	2.3	14.2
Al_2O_3	1.0	4.3	9.9	0.5	3.6	9.1	0.7	3.6
Fe_2O_3	0.1	1.2	2.9	0.1	1.3	3.0	0.1	1.3
TiO_2	n.d.	n.d.	0.1	n.d.	n.d.	0.1	n.d.	n.d.
K_2O	0.1	1.2	3.1	n.d.	n.d.	0.2	n.d.	0.5
S	n.d.	0.2	0.1	n.d.	0.1	n.d.	0.2	1.1
Sum	100	100	100	100	100	100	100	100

n = number of analyzed areas. n.d. = not detected.

The surface layer of LS had a different morphology and elemental composition as compared to the bulk of the sample (as can be seen in Figure 4 and Table 3, respectively). The thickness of the surface layer was on average 251 ± 106 µm (*n* = 24). The layer seldom covered the whole limestone surface, suggesting that the surface impurities only stuck on some parts of the surface, e.g., cavities, or that it was spalled off by abrasion or attrition during processing such as crushing, sieving, and transportation.

The SEM analysis showed that the surface layer comprised Ca-rich grains up to 300 µm, surrounded by a matrix of much smaller grains. In Figure 4a (bottom), the main surface layer impurities (Si, Al, Mg, Fe, and K) are highlighted in turquoise and Ca in red. As indicated by the coloring, a surface layer with different levels of Ca was present. In Table 3, the relative average elemental composition, expressed as oxides, of areas 1, 2, and 3 for LS is presented. In area 1, the CaO content was on average 95 wt.-%, in area 2 it was 79 wt.-% and in area 3 the CaO content was on average 55 wt.-%.

The phase composition determined by XRD and subsequent quantitative analysis of QC and $LS_{washing\ residue}$ is presented in Table 4. The diffractograms with main peaks marked are presented in Figure 5, and the list of ICSD references used for the quantification are presented in Appendix A.

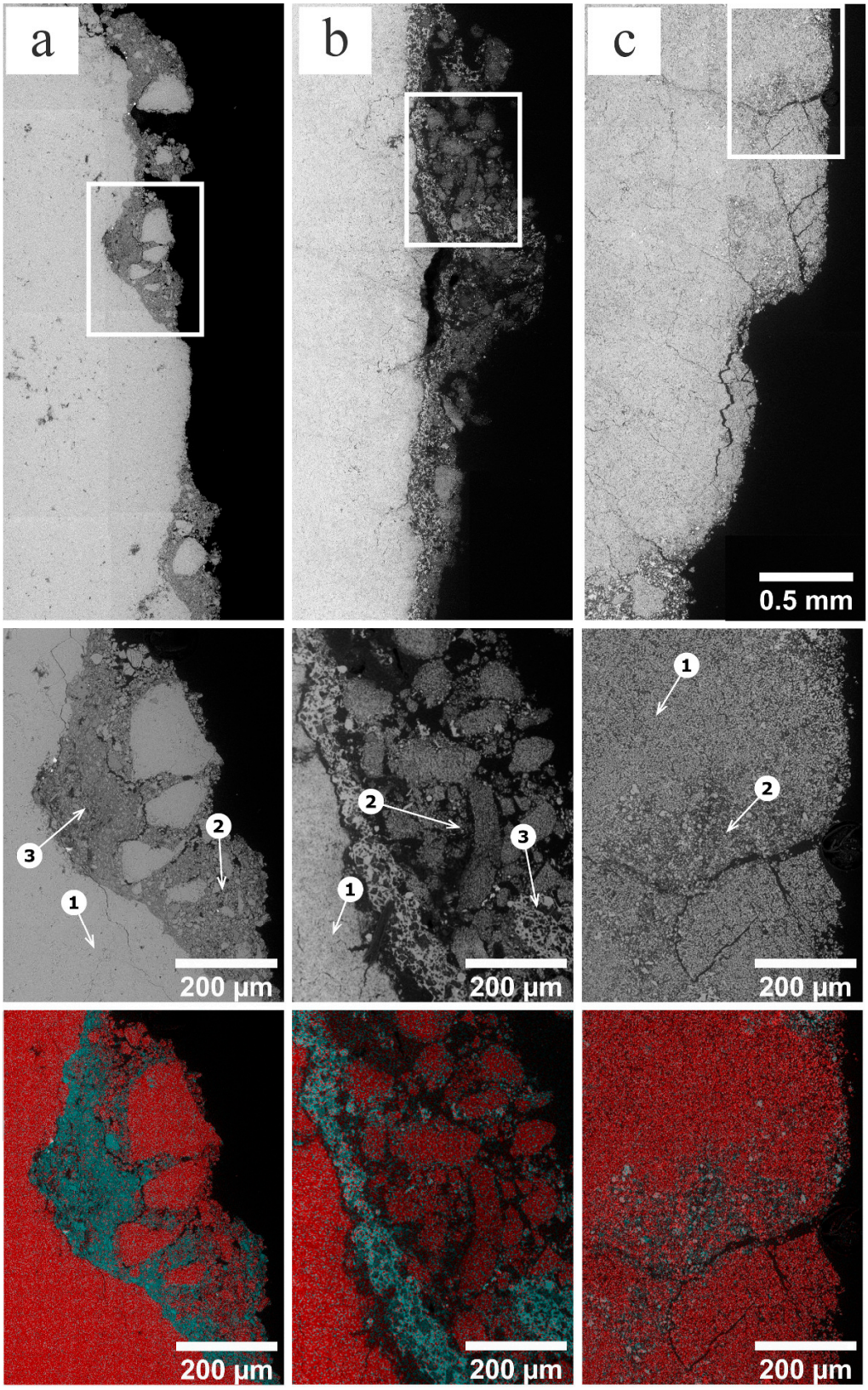

Figure 4. (**Top**) Stitched large area image of LS (**a**), LPQ (**b**), and IPQ (**c**) (mag, 300×). (**Middle**) Zoomed-in section on the surface layer: (1) bulk morphology of limestone/quicklime, (2) coarse-grained surface, (3) fine-grained surface (mag, 400×). (**Bottom**) Surface layer impurities illustrated in turquoise and Ca illustrated in red. Determined with EDX elemental mapping.

Table 4. Rietveld refinement of identified phases determined with XRD (wt.-%).

		LS	QC	LPQ	IPQ
Formula	**Mineral Name**	**Washing Residue**	**Bulk**	**Surface Layer**	**Surface Layer**
$CaCO_3$	Calcite	86	23	-	-
SiO_2	Quartz	<1	1	-	-
$CaMg(CO_3)_2$	Dolomite	12	-	-	-
$Ca(0.67Mg, 0.33Fe)(CO_3)_2$	Ferroan Dolomite	-	20	-	-
$KAl_4Si_2O_9(OH)_3/KAl_2(AlSi_3O_{10})(OH)_2$	Illite/Muscovite	2	38	-	-
$(Mg_{11.148}Fe_{0.852})((Si_{4.99}Al_{3.01})O_{20}(OH)_{16})$	Chlorite	<1	8	-	-
$K_{0.94}Na_{0.06}Si_{3.05}Al_{0.95}O_8/NaSi_3Al_{0.91}O_8$	Microcline/Albite	-	9	-	-
FeS_2	Pyrite	-	2	-	-
TiO_2	Rutile	-	<1	-	-
CaO	Lime	-	-	20	82
MgO	Periclase	-	-	15	3
Ca_2SiO_4	Larnite	-	-	12	10
$Ca(OH)_2$	Portlandite	-	-	<1	<1
$Ca_2Al_2SiO_7$	Gehlenite	-	-	23	-
$Ca_2MgSi_2O_7$	Åkermanite	-	-	3	-
$Ca_3Mg(SiO_4)_2$	Merwinite	-	-	27	4
Sum		101	101	101	100

The phase composition of QC consisted of a lower concentration of Calcite as compared to the $LS_{washing\ residue}$ (23 wt.-% compared to 86 wt.-%). Instead, QC contained Quartz (<1 wt.-%), Illite/Muscovite (38 wt.-%), Chlorite (8 wt.-%), Feldspar (9 wt.-%), Pyrite (2 wt.-%), Rutile (<1 wt.-%), and Ferroan Dolomite (20 wt.-%). In Ferroan Dolomite, up to 33 mol-% of Mg can be substituted with Fe. In $LS_{washing\ residue}$, Calcite was determined as the main phase (86 wt.-%) with minor contributions from Dolomite (12 wt.-%), Illite/Muscovite (2 wt.-%), Quarts (<1 wt.-%), and Chlorite (<1 wt.-%). The identified phases show that the composition of the surface impurities was similar to that of the QC, suggesting that QC is the origin of the fine material attached to the surface of the pebbles.

Some differences between the average elemental composition based on the XRF analysis and the XRD analysis of the QC were present. In the XRD analysis, back-calculations were used to evaluate the accuracy of the XRD analysis by recalculating the composition to pure oxides. According to back-calculations, the Al_2O_3 content was overestimated, and the SiO_2 and Fe_2O_3 content was underestimated compared to the XRF analysis for QC. However, some Al can be substituted with Fe and Si as a solid solution in Illite/Muscovite and Chlorite. In addition, components below the detection limit of XRD are another factor that can contribute to the differences seen in the XRD and XRF analysis. Furthermore, no attempt was made to distinguish between Illite and Muscovite, as they are closely related and produce similar diffractograms. Both Microcline and Albite were used to explain some minor peaks around 24°, and possibly, a feldspar solid solution between the two endmembers was present. The diffractogram and main identified peaks are presented in Figure 5.

3.3. Morphology, Elemental Distribution, and Phase Composition of Quicklimes

The relative average elemental composition of the surface layer of LPQ and IPQ are presented in Table 3. It was determined with SEM/EDX on an oxygen, chlorine, and carbon-free basis and expressed as oxides. Area 1, 2, and 3 represent different morphologies: 1 represents bulk quicklime, 2 represents coarse-grained surface impurities and 3 represents fine-grained surface impurities. These morphologies are visualized in Figure 4b,c (middle).

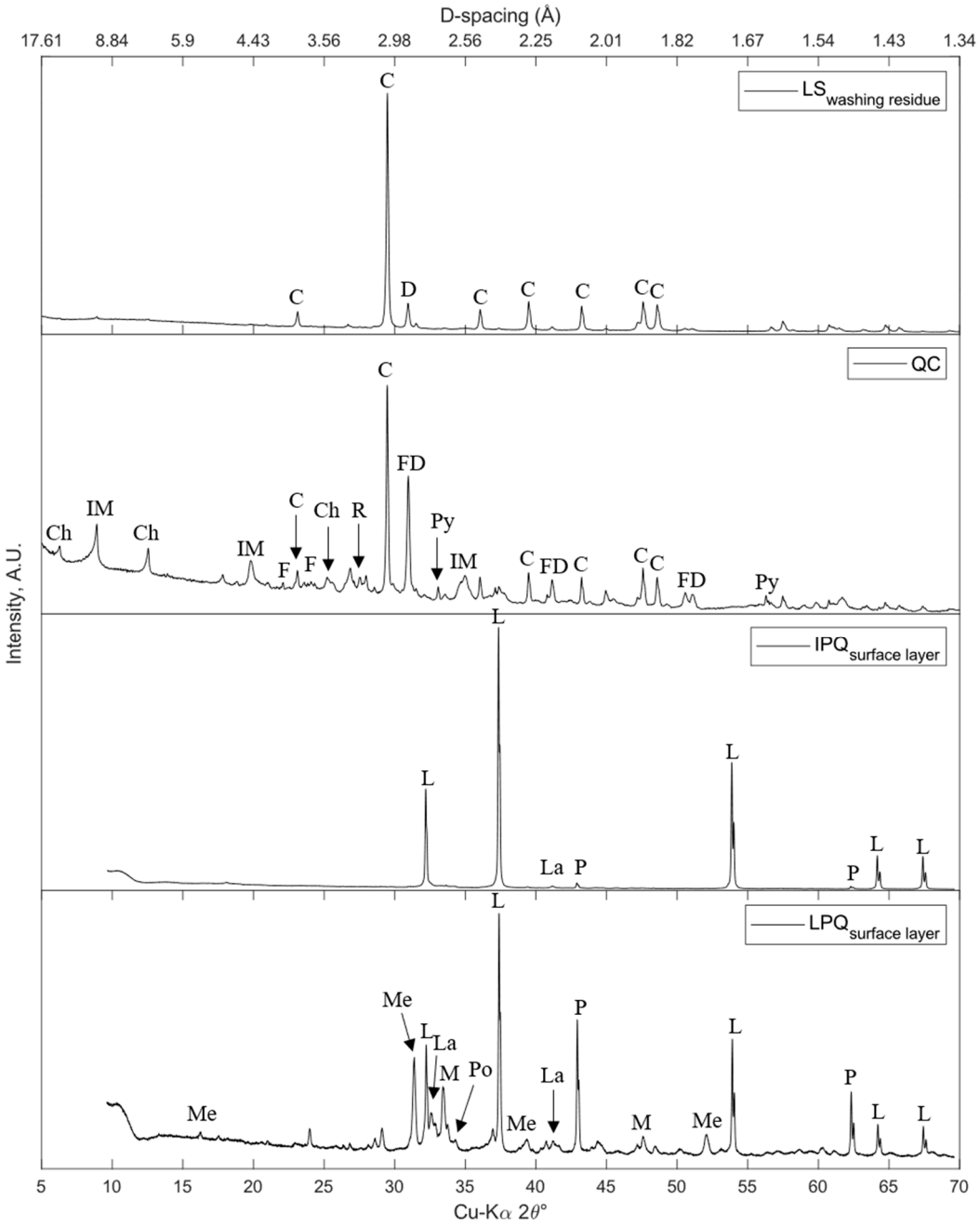

C: Calcite ($CaCO_3$)
D: Dolomite ($CaMg(CO_3)_2$)
FD: Ferroan Dolomite ($Ca(0.67Mg, 0.33Fe)(CO_3)_2$)
IM: Illite ($KAl_4Si_2O_9(OH)_3$)/Muscovite ($KAl_2(AlSi_3O_{10})(OH)_2$)
Ch: Chlorite ($(Mg_{11.148}Fe_{0.852})((Si_{4.99}Al_{3.01})O_{20}(OH)_{16})$)
F: Feldspar ($K_{0.94}Na_{0.06}Si_{3.05}Al_{0.95}O_8$/$NaSi_3Al_{0.91}O_8$)
Py: Pyrite (FeS_2)
R: Rutile (TiO_2)
L: Lime (CaO)
M: Merwinite ($Ca_3Mg(SiO_4)_2$)
P: Periclase (MgO)
La: Larnite (Ca_2SiO_4)
Me: Melilite ($Ca_2Al_2SiO_7$/$Ca_2MgSi_2O_7$)
Po: Portlandite ($Ca(OH)_2$)

Figure 5. XRD-diffractograms presented between 5 and 70 2θ° of $LS_{washing\ residue}$, bulk QC, and surface layers of IPQ and LPQ. The main peaks of the identified phases are marked.

3.3.1. LPQ

Figure 4b (top) exemplifies the morphology of the surface area of LPQ, and a surface layer with up to 700 µm thickness was determined. In Figure 4b (bottom), Ca is marked in red, and the main impurities Mg, Al, Si, and Fe are presented in turquoise. The average elemental composition expressed as oxides and exemplified by areas 1, 2, and 3 are presented in Table 3. In area 1 the CaO content was on average 97 wt.-%; in area 2, it was 83 wt.-%; and in area 3, it was 49 wt.-%. For area 3, the MgO content was 21 wt.-%, SiO_2 content was 18 wt.-%, and Al_2O_3 content was 9 wt.-%. A zoomed-in section of area 3 is presented in Figure 6. It shows a semi-melted matrix consisting of mainly Ca, Si, and Al surrounding magnesium-rich crystals of an approximate size of 10–30 µm.

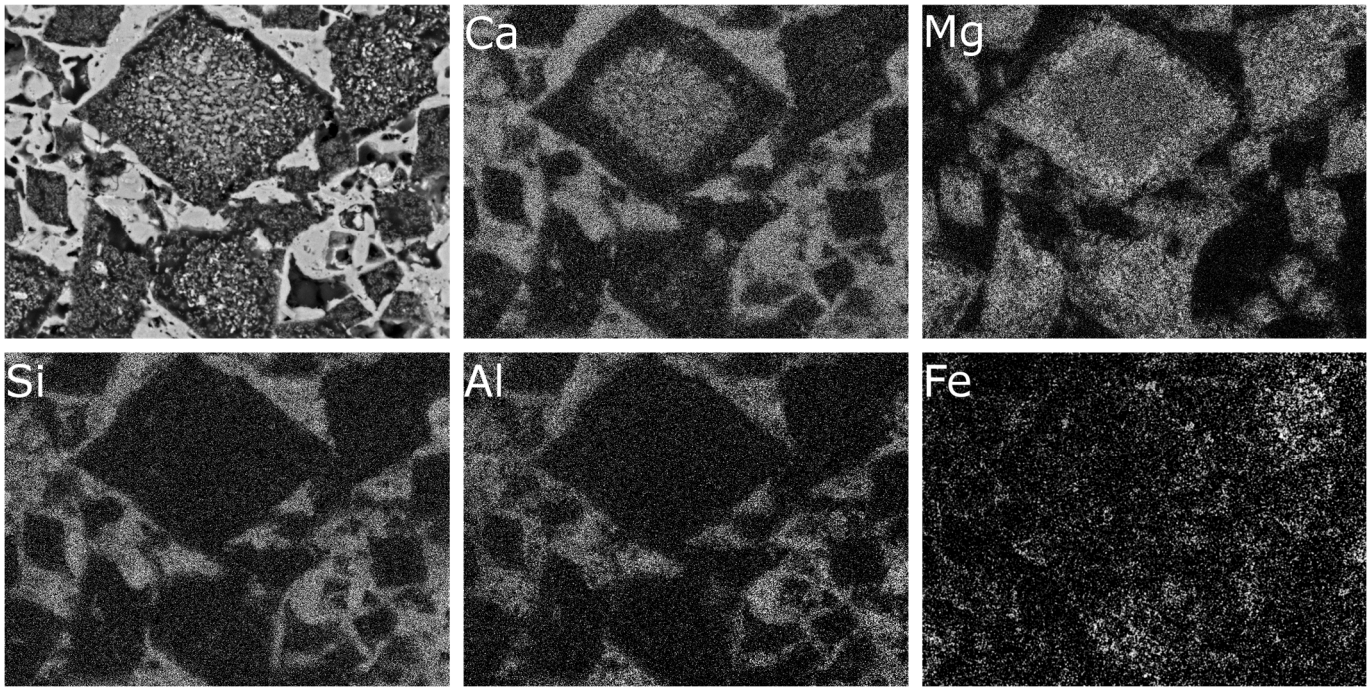

Figure 6. Upper left: SEM-BSE image of a detail in the surface layer of LPQ, area 3 in Figure 4. Others: elemental maps of Ca, Mg, Si, Al, and Fe. Field of view = 75 µm.

The phase composition determined by XRD and subsequent qualitative and quantitative analyses of LPQ are summarized in Table 4, and the diffractogram with main peaks marked are presented in Figure 5. The lime (CaO) concentration of the surface layer of LPQ was 20 wt.-%, and the main impurities Si, Al, and Mg reacted with CaO, forming Larnite (Ca_2SiO_4), Melilite (Ca_2MgSiO_7/$CaAl_2Si_2O_7$), and Merwinite ($Ca_3Mg(SiO_4)_2$). All the above-mentioned phases are unwanted and reduce the free CaO and thus the quality of the product.

3.3.2. IPQ

Figure 4c (top) exemplifies the morphology of the surface layer of IPQ. No distinctive surface impurities are visible; however, coarser areas were present but not limited to the surface region. Figure 4c (bottom) shows the impurities (Si, Al, Mg, and S) in turquoise and Ca in red. Coarsening was noted and further highlighted as "2" in Figure 4c (middle). The average elemental composition expressed as oxides and exemplified by areas 1 and 2 are presented in Table 3. In area 1, the CaO content was on average 95 wt.-%, and in area 2, it was on average 76 wt.-%.

Impurities present in clay minerals, e.g., Si and Al, were found on the surface and dispersed within the quicklime matrix—see Figure 4c (middle)—indicating that it is not related to the heterogeneous clay layers found in the quarry but originated from the

homogeneous distribution of impurities. However, it was not possible to determine if the impurities originated from heterogeneous or homogeneous dispersed material.

The phases determined by XRD and subsequent quantitative analysis of the surface layer of IPQ are presented in Table 4; the diffractogram with main peaks marked is presented in Figure 5. Lime was identified as the main phase, and Larnite, Merwinite, Periclase (MgO), and Portlandite ($Ca(OH)_2$) were also identified. Both Merwinite and Larnite lower the free CaO by diluting and reacting with CaO. Considering the operating temperatures and material flows of the kiln, it is feasible to assume that the $Ca(OH)_2$ is a reaction product of CaO hydration in the cooling zone of the kiln and during sampling, storage, transport, and preparation of the samples before the analysis. Furthermore, the absence of Hatrurite (Ca_3SiO_5) indicates that the temperature in the shaft kiln was below that of Hatrurite formation [15].

Some Illite/Muscovite was identified as the main clay mineral of the surface region of LS; see Table 4. Illite/Muscovite contains some K, also present in the XRF analysis of $LS_{washing\ residue}$ and the EDX analysis of the surface layer of LS. Illite decomposes at around 950 °C [25], and according to Aboufadil et al. [26], the presence of calcium can prohibit the formation of high-temperature K-feldspar, Sanidine, after decomposition. A possible explanation for the low K_2O content in the EDX analysis of calcined material (LPQ area 3, 0.2 wt.-% K_2O and IPQ area 2, 0.5 wt.-% K_2O) is the decomposition of Illite followed by the evaporation of K. This needs to be further investigated in terms of possible effects on kiln operation.

3.4. Overall Quality Assessment

The amount of surface impurities was quantified based on the weight of the washed limestone and washing residue. Although the surface layer was estimated to consist of 1.2 wt.-% of the total input to the kiln feed, it represented 4% of the total load of impurities, expressed as oxides. However, the overall assessment of the LPQ and IPQ (SEM/EDX and XRD analysis) indicates that the surface layer was removed to a large extent from the IPQ during processing, for example, through attrition between pebbles and abrasion with refractory surfaces in the kiln.

The removed layer can form small particles, readily suspendable within the gas flow, and eventually, at least in part, exiting the kiln with the flue gases, thus not influencing the quality of the quicklime pebbles.

Another possible fate of the surface impurities is a contribution to build-ups on the walls and in the ring channel. The clay minerals Chlorite and Illite identified in the QC are expected to, at least to some extent, melt at the operation temperature of the shaft kiln [25,27,28]. For example, Irassar et al. [25] calcined Illite/Chlorite shale at 800–1100 °C and estimated that 59% was amorphous at 1100 °C. Khalfaoui et al. [27] investigated the mineral transformation in chloritic–illitic clay at 900–1075 °C and observed a glassy phase consisting of SiO_2-K_2O-Al_2O_3 above 900 °C. The effect of surface impurities on lime densification, agglomeration, and melting in shaft kilns can be discussed in terms of the "sticking tendency" (ST) as described by Vola et al. [5,29]. A raw material with high ST can lead to build-ups in shaft kilns, with costly kiln shutdown periods. The ST mechanisms in lime shaft kilns are not yet fully understood. Earlier work has shown that some limestone samples exhibit melting, and some marlstones were shown to be completely melted at 1300 °C. Furthermore, a high presence of periclase can decrease the sticking tendency via counteracting lime densification [5].

To examine the first melt temperature and the share of melt for $LS_{as\ received}$, LS_{washed}, $LS_{washing\ residue}$, and QC, multicomponent chemical equilibrium calculations were performed; the result is presented in Figure 7. For $LS_{as\ received}$ and LS_{washed}, the share of salt melt was below 1 wt.-% and was thus excluded from Figure 7. For $LS_{as\ received}$, oxide melt was predicted above 1350 °C, and for LS_{washed}, oxide melt was predicted above 1330 °C. The difference is probably due to the TiO_2 and Mn_2O_3 content in the elemental analysis of LS_{washed} that was not reported in $LS_{as\ received}$, although they were probably present to some

extent. As can be seen in Figure 7, salt melt-levels above 1 wt.-% were predicted between 800 and 840 °C and between 1020 and 1270 °C, and oxide melt was predicted above 1320 °C for $LS_{washing\ residue}$. For QC, salt melt was predicted between 870 and 1110 °C, and oxide melt was predicted above 1050 °C. QC was fully melted at 1170 °C. HaiDo et al. [30] have simulated the maximal gas temperature in PFR kilns resulting in T_{max} = 1240 °C. This is above the temperature where QC is fully melted according to equilibrium calculations. Hence, a clay particle traveling with the gas flow can be expected to be partly or fully melted, possibly contributing to build-ups.

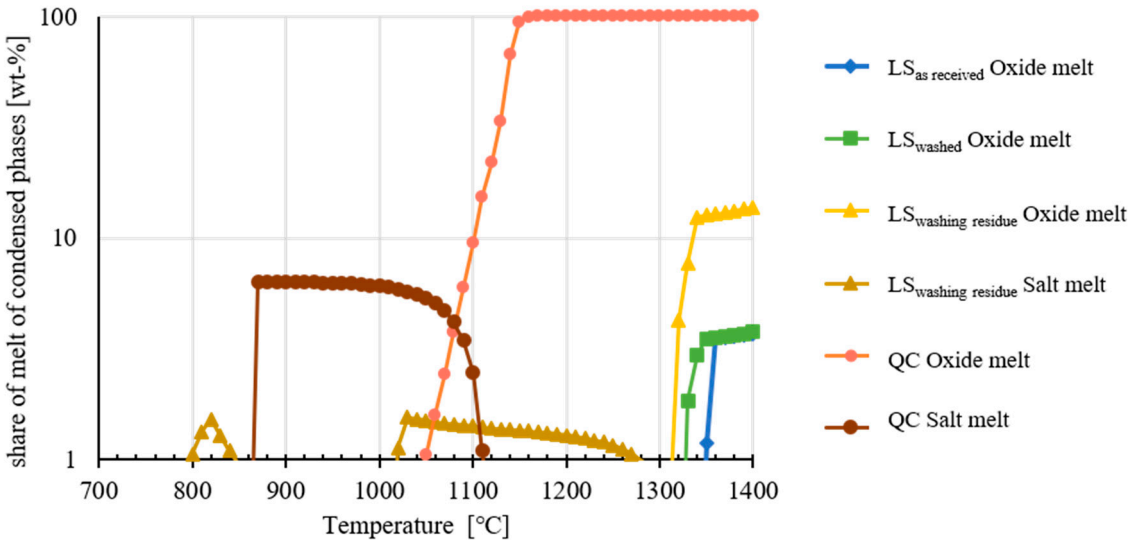

Figure 7. Share of salt melt and oxide melt of total amount of condensed phases, expressed in wt.-%.

Within a quicklime process, melted QC is expected to dissolve Ca, and the first melt temperature will rise (i.e., the composition will approach $LS_{washing\ residue}$), meaning that at a maintained temperature, the melt will re-crystallize. If this occurs on the kiln wall, it can contribute to build-ups in the shafts and ring channel. This phenomenon can be reinforced by the cyclic nature of the PFR kiln, as the material temperature is expected to vary between burning cycles. Krause et al. [2] have measured that the material temperature varies between 850 and 1050 °C near the inner wall of the burn zone of a PFR kiln, and Schlegel et al. [31] have measured that average kiln bed temperature varies between 800 and 1100 °C near the burn zone. However, no attempt was made in the present study to quantitatively determine the extent to which the clay material exits the kiln attached to the surface of the quicklime pebbles, as dust with the gas flow, or leading to build-ups. It is expected to vary with kiln parameters, such as feed fraction, temperature, heating rate, and gas velocity. This should be further investigated, for example through sampling of the lime kiln dust, shaft block formations, and ring channel build-ups.

In addition, the results can serve as a base for further investigations within the quarries, for example, by locating the main sources of quarry fine particulates with high concentrations of impurities and applying actions to reduce limestone feed product exposure to the impurities, combined with follow-up of the amount and composition of surface particulates for verification.

4. Conclusions

In this study, limestone, quarry clay, and industrially produced quicklime were sampled during moist weather causing high levels of surface impurities to adhere to the limestone. The surface layer of limestone, industrially produced quicklime, and laboratory-produced quicklime were studied in detail through XRF, SEM/EDX, and XRD analyses. Based on the results, it can be concluded that

- For the tested limestone, an accumulation of impurities was found in the surface layer. The washing residue comprised 1.2 wt.-% of the total material but contained 4% of the total impurities in limestone kiln feed;
- Elevated levels of reaction products were found on the surface of the quicklime and consisted primarily of the same elements found on the limestone surface. The XRD analysis identified Larnite, Gehlenite, Åkermanite, and Merwinite in laboratory produced quicklime, resulting in lower free CaO on the surface;
- The amount of surface impurities was lower in the industrially produced quicklime. This indicated that the limestone surface impurities were, at least to some extent, removed while the material moved through the kiln;
- The multicomponent chemical equilibrium calculations showed that the quarry clay was expected to be fully melted at 1170 °C, possibly contributing to operational problems.

Author Contributions: Conceptualization: K.S., M.C., M.E. and M.B.; Methodology: K.S., M.E. and M.B.; Formal analysis: K.S., M.C. and M.E.; Investigation: K.S. and M.C.; Visualization: K.S., M.C. and M.B.; Writing—original draft: K.S. and M.E.; Writing—review and editing: K.S., M.C., M.E. and M.B.; Supervision: M.E. and M.B.; Project administration: M.E. and M.B.; Funding acquisition: M.E. and M.B. All authors have read and agreed to the published version of the manuscript.

Funding: This research was funded by Nordkalk AB, SMA Mineral AB, Heidelberg Materials Cement Sverige AB, the Ellen, Walter, and Lennart Hesselman Foundation, the Swedish Mineral Processing Research Association—MinFo, the Industrial Doctoral School for Research and Innovation at Umeå University, and the Swedish Energy Agency.

Data Availability Statement: The raw data supporting the conclusions of this article will be made available by the authors on request.

Acknowledgments: José Aguirre Castillo is acknowledged for performing the XRD scans and providing valuable input to the XRD analysis. The authors acknowledge Multipurpose Adaptive X-ray Scattering platform (MAXS) at Umeå University for providing resources for data collection, evaluation, and technical support. The authors acknowledge Umeå Centre for Electron Microscopy (UCEM) and the National Microscopy Infrastructure (NMI), for instrument access and technical support. Kenneth Fjäder is acknowledged for providing the geological description of the limestone deposit and for providing valuable input to the mineralogical composition of the limestone and clay materials. Nordkalk AB, SMA Mineral AB, Heidelberg Materials Cement Sverige AB, the Ellen, Walter, and Lennart Hesselman Foundation, the Swedish Mineral Processing Research Association—MinFo, the Industrial Doctoral School for Research and Innovation at Umeå University, and the Swedish Energy Agency are acknowledged for project support.

Conflicts of Interest: The authors declare no conflicts of interest.

Appendix A

Table A1. Structure files used for semi-quantitative refinement of identified structures.

	ICSD Code	Structure File Reference from ICSD
Lime	52783	[32]
Portlandite	202223	[33]
Periclase	61325	[34]
Larnite	280995	[35]
α-Quartz	201354	[36]
Gehlenite	31235	[37]
Åkermanite	94142	[38]
Merwinite	26002	[39]
Microcline	34788	[40]
Albite	201649	[41]
Calcite	20179	[42]
Dolomite	31332	[43]

Table A1. *Cont.*

	ICSD Code	Structure File Reference from ICSD
Muscovite	74608	[44]
Chlorite	156707	[45]
Illite	90144	[46]
Ankerite	152200	[47]
Pyrite	53529	[48]
Rutile	31329	[49]

References

1. Schorcht, F.; Kourti, I.; Scalet, B.M.; Roudier, S.; Sancho, L.D. *Best Available Techniques (BAT) Reference Document for the Production of Cement, Lime and Magnesium Oxide*; European Commission, Joint Research Centre, Institute for Prospective Technological Studies: Brussels, Belgium, 2013; ISBN 978-92-79-32944-9.
2. Krause, B.; Liedmann, B.; Wiese, J.; Bucher, P.; Wirtz, S.; Piringer, H.; Scherer, V. 3D-DEM-CFD simulation of heat and mass transfer, gas combustion and calcination in an intermittent operating lime shaft kiln. *Int. J. Therm. Sci.* **2017**, *117*, 121–135. [CrossRef]
3. Piringer, H. Lime Shaft Kilns. *Energy Procedia* **2017**, *120*, 75–95. [CrossRef]
4. Cwik, K.; Broström, M.; Backlund, K.; Fjäder, K.; Hiljanen, E.; Eriksson, M. Thermal Decrepitation and Thermally-Induced Cracking of Limestone Used in Quicklime Production. *Minerals* **2022**, *12*, 1197. [CrossRef]
5. Vola, G.; Ardit, M.; Sarandrea, L.; Brignoli, G.; Natali, C.; Cavallo, A.; Bianchini, G.; Cruciani, G. Investigation and prediction of sticking tendency, blocks formation and occasional melting of lime at HT (1300 °C) by the overburning test method. *Constr. Build. Mater.* **2021**, *294*, 123577. [CrossRef]
6. Sandström, K. Effects of Impurities on Phase Equilibrium in Quicklime and Cement Clinker Production. PhD Thesis, comprehensive summary, Department of Applied Physics and Electronics, Umeå University, Umeå, Sweden, 2024.
7. Van Ranst, E.; Mees, F.; Bock, L.; Langohr, R. Development of a clay-rich interval above a limestone substrate in the Condroz region of southern Belgium. *Catena* **2014**, *121*, 204–213. [CrossRef]
8. Boynton, R.S. *Chemistry and Technology of Lime and Limestone*, 2nd ed.; John Wiley and Sons: Hoboken, NJ, USA, 1980.
9. Oates, J.A.H. *Lime and Limestone: Chemistry and Technology, Production and Uses*; Wiley-VCH: Weinheim, Germany, 1998.
10. Eriksson, M.; Hökfors, B.; Backman, R. The effects of oxygen enrichment and fuel composition on Rotary Kiln Lime production. *J. Eng. Technol.* **2015**, *32*, 30–43.
11. Searle, A. *Limestone & Its Products: Their Nature, Production, and Uses*; Ernest Benn Limited: London, UK, 1935.
12. Harrison, D.J.; Adlam, K.A.M. *Limestones of the Peak: A Guide to the Limestone and Dolomite Resources of the Peak District of Derbyshire and Staffordshire*; British Geological Survey—Natural Environment Research Council: London, UK, 1985; ISBN 011884444X.
13. Cox, F.C.; Bridge, D.M.; Hull, J.H. *Procedure for the Assessment of Limestone Resources*; Institute of Geological Sciences: London, UK, 1977; ISBN 9780118840309.
14. Mitchell, C. *High Purity Limestone Quest*; British Geological Survey: London, UK, 2011; pp. 48–51.
15. Eriksson, M.; Sandström, K.; Carlborg, M.; Broström, M. Impact of Limestone Surface Impurities on Quicklime Product Quality. *Minerals* **2024**, *14*, 244. [CrossRef]
16. Vola, G.; Ardit, M.; Frijia, G.; Di Benedetto, F.; Fornasier, F.; Lugli, F.; Natali, C.; Sarandrea, L.; Schmitt, K.E.; Cipriani, A. Characterization and Provenance of Carbonate Rocks for Quicklime and Dololime Production in Twin-Shaft Regenerative Kilns from the Arabian Peninsula and Neighboring Countries. *Minerals* **2023**, *13*, 500. [CrossRef]
17. Beruto, D.T.; Botter, R.; Cabella, R.; Lagazzo, A. A consecutive decomposition–sintering dilatometer method to study the effect of limestone impurities on lime microstructure and its water reactivity. *J. Eur. Ceram. Soc.* **2010**, *30*, 1277–1286. [CrossRef]
18. Wang, L.; Xue, Z.; Cai, J.; Hu, B. Relationship Between Microstructure and Properties of Limestone Calcined Rapidly at High Temperatures. *Trans. Indian Inst. Met.* **2019**, *72*, 3215–3222. [CrossRef]
19. Gates-Rector, S.; Blanton, T. The Powder Diffraction File: A quality materials characterization database. *Powder Diffr.* **2019**, *34*, 352–360. [CrossRef]
20. Bale, C.W.; Belisle, E.; Chartrand, P.; Decterov, S.A.; Eriksson, G.; Gheribi, A.E.; Hack, K.; Jung, I.H.; Kang, Y.B.; Melancon, J.; et al. FactSage thermochemical software and databases, 2010-2016. *Calphad-Comput. Coupling Ph. Diagr. Thermochem.* **2016**, *54*, 35–53. [CrossRef]
21. Lindberg, D.; Backman, R.; Chartrand, P.; Hupa, M. Towards a comprehensive thermodynamic database for ash-forming elements in biomass and waste combustion—Current situation and future developments. *Fuel Process. Technol.* **2013**, *105*, 129–141. [CrossRef]
22. Viggh, E. Modeling the Influence of Magnesium from Alternative Raw Materials on the Chemistry of Portland Cement Clinker. Ph.D. Thesis, Department of Applied Physics and Electronics, Umeå University, Umeå, Sweden, 2023.
23. *EN 459-2:2010*; Building Lime—Part 2: Test Methods. European Committee for Standardization: Brussels, Belgium, 2010; Volume 64.

24. *ASTM C25-19*; Standard Test Methods for Chemical Analysis of Limestone, Quicklime, and Hydrated Lime. ASTM International: Philadelphia, PA, USA, 2019; Volume 40.
25. Irassar, E.F.; Bonavetti, V.L.; Castellano, C.C.; Trezza, M.A.; Rahhal, V.F.; Cordoba, G.; Lemma, R. Calcined illite-chlorite shale as supplementary cementing material: Thermal treatment, grinding, color and pozzolanic activity. *Appl. Clay Sci.* **2019**, *179*, 105143. [CrossRef]
26. Aboufadil, Y.; Hajjaji, M.; Raghni, A.E.I.; Thalal, A. Heating Transformations, Technical Properties and Ceramic Suitability of Clays. *Trans. Indian Ceram. Soc.* **2013**, *72*, 201–205. [CrossRef]
27. Khalfaoui, A.; Hajjaji, M. A Chloritic-illitic clay from Morocco: Temperature–time–transformation and neoformation. *Appl. Clay Sci.* **2009**, *45*, 83–89. [CrossRef]
28. Lecomte, G.; Pateyron, B.; Blanchart, P. Experimental study and simulation of a vertical section mullite-ternary eutectic (985 °C) in the SiO_2-Al_2O_3-K_2O system. *Mater. Res. Bull.* **2004**, *39*, 1469–1478. [CrossRef]
29. Vola, G. *High-Grade Burnt Lime Products: Impact of Calcination Kinetics on Slaking Reactivity, Sticking Tendency and Blocks Formation at HT (1300 °C)*; University of Ferrara: Ferrara, Italy, 2019.
30. Haido, D.; Specht, E.; Kehse, G.; Ferri, V.; Christiansen, T.L.; Bresciani, P. Simulation of lime calcination in PFR kiln–Influence of energy input and lime throughput. *ZKG Int.* **2011**, *64*, 52–63.
31. Schlegel, T.; Padox, G. Understanding the process conditions in a parallel flow regenerative kiln. *ZKG Int.* **2016**, *69*, 56–59.
32. Smith, D.K.; Leider, H.R. Low-temperature thermal expansion of LiH, MgO and CaO. *J. Appl. Crystallogr.* **1968**, *1*, 246–249. [CrossRef]
33. Chaix-Pluchery, O.; Pannetier, J.; Bouillot, J.; Niepce, J.C. Structural prereactional transformations in $Ca(OH)_2$. *J. Solid State Chem.* **1987**, *67*, 225–234. [CrossRef]
34. Schmahl, N.G.; Eikerling, G.F. Über Kryptomodifikationen des Cu(II)-Oxids. *Z. Phys. Chem.* **1968**, *62*, 268–279. [CrossRef]
35. Toraya, H.; Yamazaki, S. Simulated annealing structure solution of a new phase of dicalcium silicate Ca_2SiO_4 and the mechanism of structural changes from α-dicalcium silicate hydrate to αL′-dicalcium silicate via the new phase. *Acta Crystallogr. Sect. B Struct. Sci.* **2002**, *58*, 613–621. [CrossRef] [PubMed]
36. Lager, G.A.; Jorgensen, J.D.; Rotella, F.J. Crystal structure and thermal expansion of α-quartz SiO_2 at low temperatures. *J. Appl. Phys.* **1982**, *53*, 6751–6756. [CrossRef]
37. Kimata, M.; Ii, N. The structural property of synthetic gehlenite, $Ca_2Al_2SiO_7$. *Neues Jahrb. Mineralogie. Abh.* **1982**, *144*, 254–267. [CrossRef]
38. Kusaka, K.; Hagiya, K.; Ohmasa, M.; Okano, Y.; Mukai, M.; Iishi, K.; Haga, N. Determination of structures of $Ca_2CoSi_2O_7$, $Ca_2MgSi_2O_7$, and $Ca_2(Mg_{0.55}Fe_{0.45})Si_2O_7$ in incommensurate and normal phases and observation of diffuse streaks at high temperature. *Phys. Chem. Miner.* **2001**, *28*, 150–166. [CrossRef]
39. Moore, P.B.; Araki, T. Atomic arrangement of merwinite, $Ca_3Mg[SiO_4]_2$, an unusual dense-packed structure of geophysical interest. *Am. Mineral.* **1972**, *57*, 1355–1374.
40. Dal Negro, A.; De Pieri, R.; Quareni, S.; Taylor, W.H. The crystal structures of nine K feldspars from the Adamello Massif (Northern Italy). *Acta Crystallogr. Sect. B* **1978**, *34*, 2699–2707. [CrossRef]
41. Wenk, H.-R.; Kroll, H. Analysis of P-1, I-1 and C-1 plagioclase structures. *Bull. Minéralog.* **1984**, *107*, 467–487. [CrossRef]
42. Borodin, V.L.; Lyutin, V.V.; Ilyukhin, V.V.; Belov, N.V. The isomorphous series calcite-otavite. *Dokl. Akad. Nauk SSSR* **1979**, *245*, 1099–1101.
43. Effenberger, H.; Kirfel, A.; Will, G. Untersuchungen zur Elektronendichteverteilung im Dolomit $CaMg(CO_3)_2$. *Mineral. Petrol.* **1983**, *31*, 151–164. [CrossRef]
44. Catti, M.; Ferraris, G.; Hull, S.; Pavese, A. Powder neutron diffraction study of 2M1 muscovite at room pressure and at 2 GPa. *Eur. J. Mineral.* **1994**, *6*, 171–178. [CrossRef]
45. Zanazzi, P.F.; Montagnoli, M.; Nazzareni, S.; Comodi, P. Structural effects of pressure on monoclinic chlorite: A single-crystal study. *Am. Mineral.* **2007**, *92*, 655–661. [CrossRef]
46. Gualtieri, A.F. Accuracy of XRPD QPA using the combined Rietveld-RIR method. *J. Appl. Crystallogr.* **2000**, *33*, 267–278. [CrossRef]
47. Reeder, R.J.; Dollase, W.A. Structural variation in the dolomite-ankerite solid-solution series: An X-ray, Mossbauer, and TEM study. *Am. Mineral.* **1989**, *74*, 1159–1167.
48. Will, G.; Lauterjung, J.; Schmitz, H.; Hinze, E. Bulk Moduli of 3d-Transition Element Pyrites Measured with Synchrotron Radiation In a New Belt Type Apparatus. *Mater. Res. Soc. Symp. Proc. MRSSP* **1984**, *22*, 49–52.
49. Walter, G. X-ray charge density study of rutile (TiO_2). *Z. Kristallographie. Cryst. Mater.* **1982**, *160*, 187–204. [CrossRef]